JAASCI
http://jaasci.com
JOURNAL OF ADVANCED APPLIED SCIENCES
e-ISSN: 2979-9759
PRENSIP
https://prensip.gen.tr

RESEARCH ARTICLE

LSTM-Based One-Day-Ahead Prediction of Ionospheric TEC Variations Associated with Major Earthquake Events in Japan and China

Secil Karatay • Seyma Avci • Buse Bayram

Kastamonu University, Faculty of Engineering and Architecture, Department of Electrical Electronics Engineering, Kastamonu/Türkiye

ARTICLE INFO

Article History
Received: 08.11.2025
Accepted: 08.12.2025
First Published: 31.12.2025

Keywords
GNSS observations
Long Short-Term Memory
Time series forecasting
Total Electron Content

ABSTRACT

Earthquakes pose significant threats to human life and infrastructure worldwide, motivating researchers to investigate potential precursory signals that may indicate impending seismic events. This study focuses on evaluating the capability of Long Short-Term Memory (LSTM) neural networks for time series prediction of IONOLAB-Total Electron Content (TEC) variations using Global Navigation Satellite Systems (GNSS) measurements during major earthquake events. We analyze IONOLAB-TEC data from 19 GNSS stations across Japan and China for four significant earthquakes: the 2011 Tohoku earthquake (Mw 9.1), the 2008 Iwate-Miyagi Nairiku earthquake (Mw 6.9), the 2008 Sichuan earthquake (Mw 7.9) and the 2010 Yushu earthquake (Mw 6.9). The LSTM model is trained using 10 days of TEC observations with 2.5-minute temporal resolution (576 observations per day) to forecast TEC values on the 11th day (earthquake day). Model performance is evaluated using three complementary metrics: Mean Squared Error (MSE), Mean Absolute Error (MAE) and Mean Absolute Percentage Error (MAPE). Results demonstrate high prediction accuracy across most stations, with MAPE values below 2% for 14 out of 19 stations. The best performances are achieved at MIZU station (MAPE: 0.45%) for the Tohoku earthquake and XIAN station (MAPE: 0.62%) for the Sichuan earthquake. Overall MSE values range from 0.0036 to 0.4493 and MAE values range from 0.0420 to 0.5014. The findings demonstrate that LSTM networks can effectively learn and reproduce temporal patterns in IONOLAB-TEC time series, accurately capturing diurnal variations and magnitude fluctuations. This study demonstrates IONOLAB-TEC prediction capability rather than earthquake precursor detection or operational early warning capability.

Please cite this paper as follows:

Karatay, S., Avci, S., & Bayram, B. (2025). LSTM-based one-day-ahead prediction of ionospheric TEC variations associated with major earthquake events in Japan and China. *Journal of Advanced Applied Sciences*, *4*(1-2), 51-66. https://doi.org/10.61326/jaasci.v4i1-2.432

1. Introduction

Earthquakes are among the most devastating natural disasters, causing significant loss of life and economic damage worldwide. Each year, seismic events affect millions of people, destroying critical infrastructure, disrupting economies and leaving lasting social impacts on affected communities. Historical records show that major seismic events, such as the 2011 Tohoku earthquake in Japan (Mw 9.1) (Namegaya et al., 2012; Uchida & Bürgmann, 2021), the 2008 Sichuan earthquake in China (Mw 7.9) (Jia et al., 2014; Peng et al., 2018), the 2010 Yushu earthquake in China (Mw 6.9) (Elliot et al., 2011; Qian & Meng, 2022) and the 2008 Iwate-Miyagi Nairiku earthquake in Japan (Mw 6.9) (Budak et al., 2024; Karatay & Gul, 2023; Karatay et al., 2025; Ogata & Toda, 2010; Samaei & Miyajima, 2022), result in catastrophic consequences affecting millions of people. The unpredictable nature of seismic events, combined with their potential for widespread destruction, motivates researchers across multiple disciplines to investigate various geophysical phenomena associated with earthquake occurrences.

Correspondence
E-mail address: skaratay@kastamonu.edu.tr

Traditional seismological methods show limited success in earthquake prediction due to the complex, nonlinear and chaotic characteristics of seismic phenomena (Mousavi & Beroza, 2023). Conventional approaches, primarily based on statistical analysis of historical seismicity patterns, geological fault studies and mechanical stress models, often fail to capture the full complexity of earthquake generation processes. This limitation stems from the multifaceted nature of seismic events, which involve intricate interactions between tectonic forces, crustal properties and various environmental factors operating across different temporal and spatial scales (Pirti & Karatay, 2025). In recent years, researchers explore various precursory signals that may indicate impending earthquakes, including changes in electromagnetic fields (Manglik et al., 2024), ground deformation (Pirti & Karatay, 2025), radon gas emissions (Nikolopoulos et al., 2024), groundwater level fluctuations (Gooya et al., 2024) and ionospheric disturbances (Akhoondzadeh, 2012; Karatay et al., 2010, 2024; Liu et al., 2004a, 2004b; Pulinets et al., 2007). Among these precursors, ionospheric anomalies detected through Global Positioning System Total Electron Content (GPS-TEC) measurements emerge as a promising area of investigation, offering advantages such as continuous monitoring capability, wide spatial coverage and relative immunity to local environmental factors that may affect ground-based measurements.

The ionosphere, a region of Earth's upper atmosphere extending from approximately 60 km to 1000 km altitude, contains a significant concentration of free electrons and ions produced primarily through solar radiation and cosmic ray ionization (Heelis & Maute, 2020). This electrically conductive layer plays a crucial role in radio wave propagation and satellite communication systems. Total Electron Content (TEC) represents the total number of electrons present along a path between a GPS satellite and a ground receiver, typically measured in TEC Units (TECU), where 1 TECU equals 10^{16} electrons per square meter (Sardón et al., 1994; Tsai & Liu, 1999). Under normal conditions, TEC values exhibit regular diurnal variations controlled by solar activity, geomagnetic conditions and seasonal changes (Karatay et al., 2017; Karatay, 2020a, 2020b). Previous studies have reported TEC anomalies in temporal proximity to major earthquakes, though the mechanisms and reliability of such observations remain subjects of ongoing scientific investigation. While the potential relationship between ionospheric variations and seismic activity continues to be explored, TEC data represents a valuable resource for studying ionospheric behavior through time series analysis and prediction methods (Li et al., 2025; Manglik et al., 2024; Nikolopoulos et al., 2024; X. Zhang et al., 2023).

Long Short-Term Memory (LSTM) networks a specialized type of Recurrent Neural Network (RNN), demonstrate remarkable capability in handling time-series data and capturing long-term dependencies in sequential patterns (Houdt et al., 2020; Hua et al., 2019; Mienye et al., 2024). Unlike conventional neural networks, which process inputs independently without memory of previous data points, LSTM networks possess memory cells that can retain information over extended periods while selectively forgetting irrelevant data, making them particularly suitable for temporal sequence analysis. This unique architecture includes input gates, forget gates and output gates that regulate information flow through careful control of what information should be stored, updated, or discarded at each time step, enabling the network to learn complex temporal patterns that may span various time scales (Lindemann et al., 2021). The ability of LSTM to model nonlinear relationships, capture temporal dependencies and extract hidden patterns from noisy time-series data makes it an ideal candidate for analyzing TEC time-series data (Budak & Gider, 2023). Furthermore, LSTM networks have demonstrated superior performance in numerous time-series forecasting applications ranging from weather prediction and financial market analysis to natural language processing and energy consumption forecasting, establishing a strong foundation for their application in geophysical time-series prediction. The application of LSTM networks to TEC data (Iluore & Lu, 2022; Xiong et al., 2021; T. Y. Yang et al., 2025) represents an innovative approach that combines space-based observations with advanced Machine Learning (ML) techniques. By analyzing temporal TEC variations and learning characteristic patterns in the data, LSTM models can potentially capture subtle trends and dependencies that might be difficult to detect through conventional statistical methods or human visual inspection. This interdisciplinary approach bridges geophysics (L. Yang et al., 2023), space physics (Nathasarma & Roy, 2023) and artificial intelligence (Cansu et al., 2023; Houdt et al., 2020), leveraging the increasing availability of high-resolution observational data with data-driven modeling techniques. The integration of Deep Learning (DL) methodologies with geophysical observations represents an important methodological advancement in ionospheric research, moving toward approaches that can effectively process and model complex time-series data (Bouktif et al., 2018).

The prediction accuracy of the LSTM model is rigorously evaluated using three standard error metrics: Mean Squared Error (MSE), Mean Absolute Error (MAE) and Mean Absolute Percentage Error (MAPE) (Wen & Li, 2023). These complementary metrics provide comprehensive insights into the model's performance from different perspectives. MSE, calculated as the average of squared differences between predicted and actual values, emphasizes larger errors and is sensitive to outliers, making it useful for identifying cases where the model produces significant mispredictions (Erken et al., 2019; Hurvich et al., 1998; Q. Zhang et al., 2017). MAE provides a linear measure of average prediction error magnitude, offering an intuitive interpretation of typical prediction accuracy in the same units as the original data

(Takyi-Aninakwa et al., 2022; Tian et al., 2018). MAPE provides an intuitive percentage-based measure of prediction accuracy that is scale-independent, enabling meaningful comparisons across different earthquake events and TEC value ranges (Meenalakshmi & Valarmathi, 2025; Tian et al., 2018). The combination of these three metrics enables a thorough quantitative assessment of the differences between predicted and actual TEC values for each seismic event, accounting for both systematic biases and random fluctuations in prediction errors.

It is important to distinguish between two related but distinct objectives in ionospheric research: (1) demonstrating the capability to accurately predict TEC time series values and (2) detecting anomalies that may serve as earthquake precursors. The present study focuses primarily on the first objective—evaluating the LSTM model's ability to learn temporal patterns and accurately forecast TEC values on earthquake days using only pre-earthquake training data. High prediction accuracy indicates that the model successfully captures the underlying temporal dynamics of TEC variations, but does not necessarily imply anomaly detection capability or validate the existence of earthquake precursors. Distinguishing normal TEC variations from true seismic precursors would require comparative analysis of prediction errors on earthquake days versus non-earthquake days, which is beyond the scope of this investigation.

In this research, we investigate the effectiveness of LSTM algorithms in predicting IONOLAB-TEC values estimated during four major seismic events: the March 11, 2011 Tohoku earthquake in Japan (Mw 9.1), the June 13, 2008 Iwate-Miyagi Nairiku earthquake in Japan (Mw 6.9), the May 12, 2008 Sichuan earthquake in China (Mw 7.9) and the April 14, 2010 Yushu earthquake in China (magnitude 6.9). These events are selected to represent diverse seismotectonic settings and different magnitude ranges, providing a varied dataset for evaluating LSTM model performance under different seismic conditions. For each earthquake event, we collect 11-day IONOLAB-TEC time-series datasets covering the period leading up to and including the day of the earthquake. The first 10 days of IONOLAB-TEC data are used as training inputs for the LSTM model, while the 11th day (the day of the earthquake) serves as the prediction target. This methodological approach allows us to systematically evaluate the model's capability to forecast IONOLAB-TEC values one day in advance based on the preceding temporal patterns in ionospheric variations.

2. Materials and Methods

Total Electron Content (TEC) is a fundamental ionospheric parameter that quantifies the total number of free electrons along the signal propagation path between a Global Navigation Satellite Systems (GNSS) satellite and a ground-based receiver. TEC is conventionally expressed as the column density of electrons within a cross-sectional area of one square meter, measured in TEC Units (TECU), where 1 TECU = 10^{16} electrons/m² (Sardón et al., 1994; Tsai & Liu, 1999). This parameter exhibits systematic variations associated with diurnal cycles, seasonal patterns, geographical location, solar activity and geomagnetic disturbances (Karatay et al., 2010, 2017; Karatay, 2020a, 2020b). The detection of TEC anomalies is extensively investigated as a potential indicator of ionospheric disturbances that may precede major seismic events.

In this study, IONOLAB-TEC are estimated for four major earthquakes, Japan (2008 and 2011) and China (2008 and 2010). IONOLAB-TEC values are estimated using the IONOLAB-TEC algorithm, which employs a Regularized Estimation (Reg-Est) technique specifically developed for robust TEC estimation from dual-frequency GNSS measurements (Arikan et al., 2003, 2004; IONOLAB, 2006; Nayir et al., 2007; Sezen et al., 2013). The Reg-Est algorithm addresses several challenges inherent in GNSS-based TEC estimation, including cycle slips, receiver bias instabilities and multipath effects. The methodology utilizes both L1 (1575.42 MHz) and L2 (1227.60 MHz) carrier phase and pseudorange measurements from GPS satellites to compute the ionospheric delay, which is then converted to vertical TEC using appropriate geometric mapping functions.

For this analysis, IONOLAB-TEC values are estimated with a temporal resolution of 2.5 minutes, providing approximately 576 observations per day for each station. This high-resolution sampling rate is suitable for detecting short-term ionospheric variations and remains computationally feasible for time series techniques. The IONOLAB-TEC time series for any GPS receiver u operating on day d can be mathematically represented as a vector:

$$\boldsymbol{x}_{u;d} = [x_{u;d}(1) \dots \dots x_{u;d}(n) \dots \dots x_{u;d}(N)]^T \quad (1)$$

where N denotes the total number of observations within the 24-hour period. For the 2.5-minute sampling interval used in this study, $N = 576$. IONOLAB-TEC is estimated 10 days before the each earthquake and the earthquake days (11 days). Geographic locations of the chosen GNSS stations are given in Table 1. Geographic locations, date, time, magnitude and depth of these earthquakes are also given in Table 2 (USGS, 1879). The location and distances of the E1, E2, E3 and E4 earthquakes and the selected GNSS stations are shown in Figure 1.

Table 1. GPS/GNSS stations used in the study with their geographical coordinates and associated earthquake events. E1: 2011 Tohoku earthquake, E2: 2008 Sichuan earthquake, E3: 2010 Yushu earthquake, E4: 2008 Iwate-Miyagi Nairiku earthquake.

Station ID	Latitude (°N)	Longitude (°E)	Earthquake
AIRA	31.65	130.59	E1 and E4
CHAN	43.59	125.44	E2 and E3
DAEJ	36.25	127.37	E2 and E3
GUAO	43.27	87.17	E2 and E3
KUNM	24.88	102.79	E2 and E3
LHAZ	29.49	91.10	E2 and E3
MIZU	38.94	141.13	E1 and E4
MTKA	35.49	139.56	E1 and E4
SHAO	30.92	121.20	E2 and E3
SMST	33.40	135.93	E1 and E4
STK2	43.33	141.84	E1 and E4
SUWN	37.09	127.05	E2 and E3
TCMS	24.65	120.98	E2 and E3
TSK2	35.92	140.08	E1 and E4
TSKB	35.92	140.08	E1 and E4
URUM	43.61	87.60	E2 and E3
USUD	35.95	138.36	E1 and E4
XIAN	34.18	109.22	E2 and E3
YSSK	46.83	142.71	E1 and E4

Table 2. Characteristics of the four earthquakes investigated in this study, including date, time (UT), epicenter coordinates, magnitude (Mw) and focal depth (USGS, 1879).

Earthquake	Date (dd.mm.yyyy)	Time (UT)	Latitude (°N)	Longitude (°E)	Magnitude (Mw)	Depth (km)
E1	11.03.2011	14.46	38.3	142.4	9.1	29
E2	12.05.2008	14.28	31.0	103.4	7.9	19
E3	14.04.2010	07.49	33.3	96.6	6.9	17
E4	13.06.2008	23.43	39.0	140.9	6.9	10

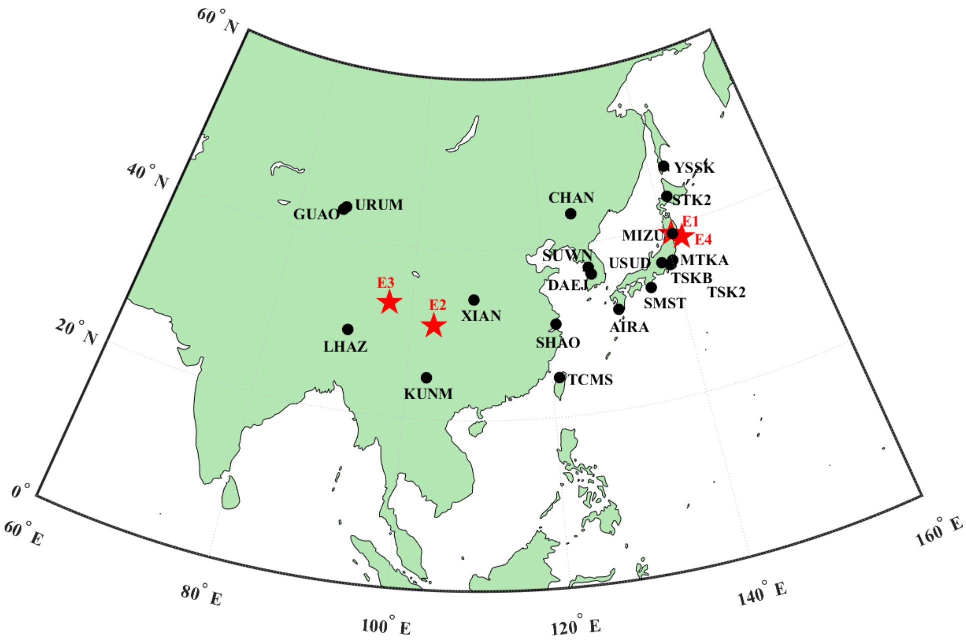

Figure 1. Geographic locations of the chosen earthquakes and GNSS stations.

Taken together, Tables 1 and 2 and Figure 1 present both the key parameters of four major earthquake events and the spatial distribution of GNSS stations located within their surrounding regions. This comprehensive dataset enables a comparative investigation of ionospheric behavior from both temporal and spatial perspectives. It also provides a robust foundation for evaluating the consistency of TEC variations under different seismic magnitudes, thereby facilitating the identification of potential pre-seismic ionospheric anomalies. In the following section, methodology employed in this study are described in detail.

2.1. Training and Testing Protocol

To ensure temporal independence and prevent data leakage, each earthquake event is analyzed independently with its own dedicated training dataset. The model is retrained from scratch for each earthquake, with no information sharing between different seismic events. This protocol guarantees that conclusions drawn for one earthquake do not influence predictions for another.

Figure 2 illustrates the temporal structure of the training and testing protocol for a representative earthquake case. The diagram shows the clear separation between the 10-day training period (days -10 to -1) and the earthquake occurrence (day 0), demonstrating how temporal independence is maintained throughout the analysis.

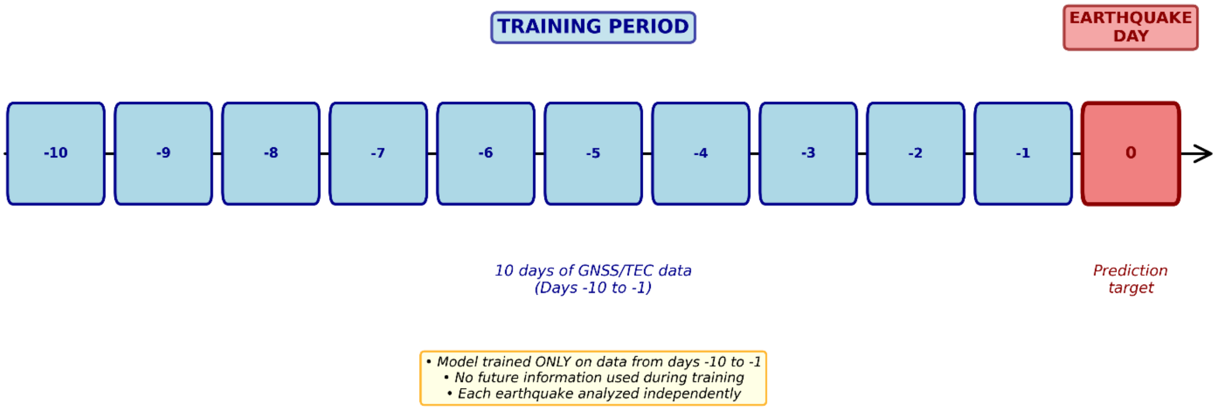

Figure 2. Schematic diagram illustrating the temporal train/test split protocol. The timeline shows the 10-day training window (days -10 to -1) preceding the earthquake event (day 0), demonstrating the temporal independence of the prediction framework.

The temporal relationship between training data and earthquake occurrence is strictly controlled. For each earthquake event occurring on day 0, the training window consists of 10 days of GNSS coordinate time series data collected immediately before the earthquake, specifically from day -10 to day -1 relative to the earthquake date. The model then makes predictions for day 0 (the earthquake day) using only information from the preceding 10-day period. This ensures that the model never has access to future information during training, maintaining strict temporal ordering where training data always precedes the target prediction date.

2.2. Mathematical Model of LSTM Based Time Series Algorithm

The study presents the LSTM-based forecasting model developed for prediction of IONOLAB-TEC data obtained for four major earthquakes in Japan and China. The model architecture consists of data preprocessing, LSTM network structure and optimization algorithm and performance evaluation metrics. The proposed system operates on IONOLAB-TEC time series data collected from multiple GNSS stations, where $w \in \{1, 2, \ldots, W\}$ denotes the station index with W being the total number of stations, $d \in \{1, 2, \ldots, 11\}$ represents the day index, N is the total number of time steps per day and $x_{w,d}(n)$ is the IONOLAB-TEC value at the n-th time step on day d for station w. The dataset is partitioned into training and testing subsets following a temporal split strategy, where the first 10 days constitute the training set and the 11th day serves as the testing set for model validation.

The training dataset comprises the first 10 days of observations, formulated as:

$$\boldsymbol{x}_{train} = [\boldsymbol{x}_{w,1}, \boldsymbol{x}_{w,2}, \ldots, \boldsymbol{x}_{w,10}] \tag{2}$$

This multi-day data is vectorized into a single sequential representation as:

$$\boldsymbol{X}_{train}^{vec} = [x_{w,1}(1), x_{w,2}(2), \ldots, x_{w,10}(N)]^T \tag{3}$$

The test dataset consists of the 11th day observations, expressed as:

$$\boldsymbol{X}_{test} = x_{w,11} = [x_{w,11}(1), \ldots, x_{w,11}(N)]^T \tag{4}$$

To ensure numerical stability and accelerate convergence during training, normalization is applied to the training data. The mean and standard deviation for station w are computed as:

$$\mu_w = \frac{1}{10N}\sum_{d=1}^{10}\sum_{n=1}^{N} x_{w,d}(n) \quad (5)$$

$$\sigma_w = \sqrt{\frac{1}{10N}\sum_{d=1}^{10}\sum_{n=1}^{N}(x_{w,d}(n) - \mu_w)^2} \quad (6)$$

The normalized training data is then obtained through the transformation:

$$\hat{x}_{w,d}(n) = \frac{x_{w,d}(n) - \mu_w}{\sigma_w} \quad (7)$$

The LSTM network is trained using sequential input-output pairs constructed from the normalized data. The input sequence is defined as (Houdt et al., 2020; Hua et al., 2019; Mienye et al., 2024):

$$\boldsymbol{X}_{LSTM} = [\hat{x}_w(1), \hat{x}_w(2), \ldots, \hat{x}_w(10N-1)]^T \quad (8)$$

while the corresponding target sequence is:

$$\boldsymbol{Y}_{LSTM} = [\hat{x}_w(2), \hat{x}_w(3), \ldots, \hat{x}_w(10N)]^T \quad (9)$$

This formulation establishes a one-step-ahead prediction task where each input $\hat{\boldsymbol{x}}_w(t)$ is mapped to the subsequent value $\hat{\boldsymbol{x}}_w(t+1)$.

The core of the LSTM architecture consists of memory cells with gating mechanisms that regulate information flow through four key operations at each time step t. Figure 3 illustrates these components visually. The mathematical formulation proceeds as follows (Houdt et al., 2020; Hua et al., 2019; Mienye et al., 2024):

$$\boldsymbol{f}_t = \sigma(\boldsymbol{W}_f \cdot [\boldsymbol{h}_{t-1}, \hat{\boldsymbol{x}}_w(t)] + \boldsymbol{b}_f) \quad (10)$$

where σ denotes the sigmoid activation function, $\boldsymbol{W}_f$ is the weight matrix and $\boldsymbol{b}_f$ is the bias vector. The forget gate (Equation 10) determines which information from the previous cell state $\boldsymbol{C}_{t-1}$ should be discarded. The input gate controls the incorporation of new information, expressed as:

$$\boldsymbol{i}_t = \sigma(\boldsymbol{W}_i \cdot [\boldsymbol{h}_{t-1}, \hat{\boldsymbol{x}}_w(t)] + \boldsymbol{b}_i) \quad (11)$$

A candidate cell state is generated using:

$$\widehat{\boldsymbol{C}}_t = \tan h\,(\boldsymbol{W}_c \cdot [\boldsymbol{h}_{t-1}, \hat{\boldsymbol{x}}_w(t)] + \boldsymbol{b}_c) \quad (12)$$

where $tanh$ is the hyperbolic tangent activation function.

The cell state is updated by combining the previous cell state with the new candidate information:

$$\boldsymbol{C}_t = \boldsymbol{f}_t \odot \boldsymbol{C}_{t-1} + \boldsymbol{i}_t \odot \widehat{\boldsymbol{C}}_t \quad (13)$$

where $\odot$ represents element-wise multiplication. The output gate regulates the final hidden state output, calculated as:

$$\boldsymbol{o}_t = \sigma(\boldsymbol{W}_o \cdot [\boldsymbol{h}_{t-1}, \hat{\boldsymbol{x}}_w(t)] + \boldsymbol{b}_o) \quad (14)$$

The hidden state, which serves as the memory representation of the sequence, is then computed as (Houdt et al., 2020; Hua et al., 2019; Mienye et al., 2024):

$$\boldsymbol{h}_t = \boldsymbol{o}_t \odot \tan h\,(\boldsymbol{C}_t) \quad (15)$$

In this implementation, the hidden state is a 50-dimensional vector, i.e.,

$$\boldsymbol{h}_t \in \mathbb{R}^{50}. \quad (16)$$

These five equations (10-15) work together to enable selective information retention: the forget gate (10) controls what to discard from memory, the input gate (11) and candidate state (12) determine what new information to add, the cell state update (13) combines these decisions and the output gate (14-15) regulates what information to expose to the next layer. This gating mechanism enables the LSTM to capture long-term temporal dependencies in the TEC time series.

The complete LSTM architecture consists of a single LSTM layer with 50 hidden units, followed by a fully connected (dense) layer that maps the 50-dimensional hidden state to a single output value. The choice of 50 hidden units was determined through preliminary experiments comparing architectures with 25, 50, 100 and 200 units. The 50-unit configuration demonstrated the best balance between model capacity and generalization performance: smaller networks (25 units) showed underfitting with inability to capture the full complexity of diurnal TEC patterns, while larger networks (100+ units) provided no significant performance improvement while increasing computational cost and potential overfitting risk. No dropout regularization or other explicit regularization techniques are applied, as the relatively small network capacity (single LSTM layer with 50 units) and the continuous nature of the time series data provide implicit regularization. The training process uses the entire 10-day dataset without a separate validation split, as each earthquake event is analyzed independently and the focus is on demonstrating prediction capability rather than hyperparameter tuning across multiple architectures.

The LSTM layer is followed by a fully connected layer that maps the hidden state to the prediction space (Houdt et al., 2020; Hua et al., 2019; Mienye et al., 2024). The normalized prediction at time step t+1 is obtained through:

$$\hat{x}_w(t+1) = \boldsymbol{W}_{fc} \cdot \boldsymbol{h}_t + \boldsymbol{b}_{fc} \quad (17)$$

where $\boldsymbol{W}_{fc}$ and $\boldsymbol{b}_{fc}$ are the weight matrix and bias of the fully connected layer, respectively.

For predictions on the 11th day test data, the normalized test sequence undergoes the same transformation and is fed into the trained LSTM network. The network produces normalized predictions which are subsequently transformed back to the original scale through denormalization:

$$x_{w,11}(n) = \hat{x}_{w,11}(n) \cdot \sigma_w + \mu_w \quad (18)$$

where $\hat{x}_{w,11}(n)$ represents the predicted TEC value for the nth time step of the 11th day at station w.

The performance of the forecasting system is quantified using three standard regression metrics. The Mean Squared Error (MSE) measures the average squared difference between predictions and actual values (Erken et al., 2019; Hurvich et al., 1998; Rohit Deo, 1998; Q. Zhang et al., 2017):

$$MSE_w = \frac{1}{N}\sum_{n=1}^{N}(\hat{x}_{w,11}(n) - x_{w,11}(n))^2 \tag{19}$$

The Mean Absolute Error (MAE) provides a linear measure of prediction accuracy data (Takyi-Aninakwa et al., 2022; Tian et al., 2018):

$$MAE_w = \frac{100}{N}\sum_{n=1}^{N}\left|\hat{x}_{w,11}(n) - x_{w,11}(n)\right| \tag{20}$$

The Mean Absolute Percentage Error (MAPE) expresses the error as a percentage (Meenalakshmi & Valarmathi, 2025; Tian et al., 2018):

$$MAPE_w = \frac{100}{N}\sum_{n=1}^{N}\left|\frac{\hat{x}_{w,11}(n) - x_{w,11}(n)}{x_{w,11}(n)+\epsilon}\right| \tag{21}$$

where $\epsilon = 2.22 \times 10^{-16}$ is a small constant added to prevent division by zero.

The network parameters are optimized by minimizing the Mean Squared Error loss function over the training sequence:

$$L(\theta) = \frac{1}{10N-1}\sum_{t=1}^{10N-1}(\hat{x}_w(t+1) - x_w(t+1))^2 \tag{22}$$

where θ represents all trainable parameters of the network. The optimization is performed using the Adam algorithm, which adapts the learning rate for each parameter. The parameter update rule is given by:

$$\theta_{k+1} = \theta_k - \alpha \cdot \frac{\widehat{m}_k}{\sqrt{\hat{v}_k} + \epsilon} \tag{23}$$

where $\alpha = 0.005$ is the initial learning rate, $\widehat{m}_k$ and $\hat{v}_k$ are the bias-corrected first and second moment estimates, respectively. The network is trained for 100 epochs with a gradient threshold of 1 to prevent gradient explosion, a common issue in recurrent neural networks. To ensure clarity and consistency, Table 3 provides a complete reference of all mathematical symbols and notation used in the model formulation below. The model consists of data preprocessing, LSTM network structure, optimization algorithm and performance evaluation metrics.

Table 3. Mathematical notation and symbol definitions of the algorithm.

Component	Symbol	Value	Explanation
Number of LSTM layers	—	1	A single layer is sufficient for producing the hidden state $h_t \in \mathbb{R}^{50}$
Hidden units	$dim(\boldsymbol{h}_t)$	50	Matches Eq. (16), ensuring a 50-dimensional hidden state
Sequence input	$x_{u;d}(n)$	576 samples × 10 days	Consistent with Eq. (3), representing the full training sequence.
Normalized input	$\hat{x}_{w,d}(n)$	Z-score	Uses mean μ_w and standard deviation σ_w as defined in Eqs. (5)–(7)
Prediction	$\hat{x}_{w,d}(n+1)$	One-step ahead	Matches Eqs. (17)–(18) for LSTM output
Cell state	$\boldsymbol{C}_t$	—	Internal LSTM memory state (Eq. (13))
Hidden state	$\boldsymbol{h}_t$	50-dimensional	Defined in Eqs. (15)–(16)
Forget gate	$\boldsymbol{f}_t = \sigma(\cdot)$	—	As in Eq. (10)
Input gate	$\boldsymbol{i}_t = \sigma(\cdot)$	—	As in Eq. (11)
Candidate state	$\widehat{\boldsymbol{C}}_t = \tan h(\cdot)$	—	As in Eq. (12)
Output gate	$\boldsymbol{o}_t = \sigma(\cdot)$	—	As in Eq. (14)
Optimizer	—	Adam	Uses the update rule in Eq. (23)
Learning rate	α	0.00	Standard Adam learning rate; stable for TEC series
Loss function	$L(\theta)$	MSE	Matches the objective function in Eq. (22)
Batch size	—	5,760	Full-sequence training preserves temporal continuity
Epochs	—	100	Ensures stable convergence across stations
Training window	$d = -10 \ldots -1$	10 days	Follows the dataset definition in Eqs. (2)–(4)
Sampling interval	$d = 1 \ldots 576$	2.5 minutes	Matches Eq. (1) where $N = 576$
Denormalization	$x = \hat{x}\sigma + \mu$	—	As defined in Eq. (18)

The training process uses batch gradient descent with the entire training sequence (5,760 observations per station) processed as a single batch, given the moderate dataset size. This approach ensures that temporal dependencies across the full 10-day training window are preserved during backpropagation through time. The initial learning rate is set to $\alpha = 0.001$, which is the standard default value for the Adam optimizer and has been extensively validated for time series forecasting tasks in the literature. Preliminary experiments confirmed stable convergence at this learning rate across all stations and earthquake events, eliminating the need for manual tuning.

The fixed 100-epoch training duration was selected based on preliminary convergence analysis. Observation of loss curves across multiple stations showed that the Mean Squared Error (MSE) loss function typically stabilized within 60-80 epochs, with negligible improvement beyond 100 epochs. The 100-epoch limit ensures complete convergence across all stations and events while maintaining consistency in the experimental protocol. Early stopping was not implemented to avoid introducing additional hyperparameters that would require validation data and to maintain uniformity across all earthquake analyses. The hyperparameter configuration prioritizes simplicity and reproducibility: the 50-unit hidden dimension provides sufficient capacity to capture TEC temporal patterns without overfitting, the 10-day training window balances temporal context with computational efficiency and the 2.5-minute sampling interval (576 observations/day) preserves the detailed structure of diurnal TEC variations.

To enhance methodological transparency and reproducibility, Table 4 provides a comprehensive summary of all LSTM model hyperparameters and architectural choices. Each hyperparameter is accompanied by its corresponding value and a brief justification explaining the rationale behind the selection. The hyperparameter configuration prioritizes simplicity, reproducibility and computational efficiency while maintaining sufficient model capacity to capture the complex temporal dynamics of ionospheric TEC variations.

Table 4. LSTM model hyperparameters and architecture configuration.

Hyperparameter	Value	Justification
Architecture		
Number of LSTM layers	1	Single layer sufficient for univariate time series; prevents overfitting with limited training data
Hidden units per LSTM layer	50	Balances model capacity with dataset size; captures diurnal patterns without excessive parameters
Output layer	Fully connected (Dense)	Maps 50-dimensional hidden state to single TEC prediction value
Training Configuration		
Batch size	Full sequence (5,760 observations)	Entire 10-day sequence processed together; suitable for moderate dataset size
Number of epochs	100	Ensures convergence across all stations; preliminary tests showed stabilization within this range
Optimizer	Adam	Adaptive learning rates for each parameter; robust performance for time series tasks
Initial learning rate (α)	0.001	Standard Adam default; effective for TEC prediction without manual tuning
Gradient clipping threshold	1.0	Prevents gradient explosion in recurrent networks
Regularization		
Dropout	None	Small network capacity and continuous time series nature do not require explicit regularization
L1/L2 regularization	None	Single LSTM layer with 50 units provides implicit regularization through architecture
Data Configuration		
Training window	10 days	Balances temporal context (captures weekly patterns) with computational efficiency
Sampling interval	2.5 minutes	576 observations/day; preserves detailed diurnal TEC structure
Validation split	None	Each earthquake analyzed independently; focus on prediction capability demonstration
Early stopping	Not applied	Maintains consistency across analyses; avoids additional hyperparameter complexity
Normalization		
Method	Z-score standardization	Equation (5)-(7); ensures numerical stability and training convergence

As shown in Table 4, the architectural and training choices reflect a balance between model complexity and practical constraints. The single-layer LSTM architecture with 50 hidden units provides adequate representational capacity for univariate time series forecasting without the risk of overfitting that might arise from deeper or wider networks given the limited training data per earthquake event. The decision to process the entire 10-day sequence as a single batch, rather than using mini-batch training, is justified by the moderate dataset size and ensures that temporal dependencies across the full training window are preserved during backpropagation through time.

Figure 3 presents a schematic diagram of the complete LSTM architecture, illustrating the sequential data flow from raw TEC input through normalization, the LSTM layer with its internal gating mechanisms, the fully connected output layer and finally denormalization to produce the predicted TEC value. The diagram also summarizes the key training configuration parameters detailed in Table 3.

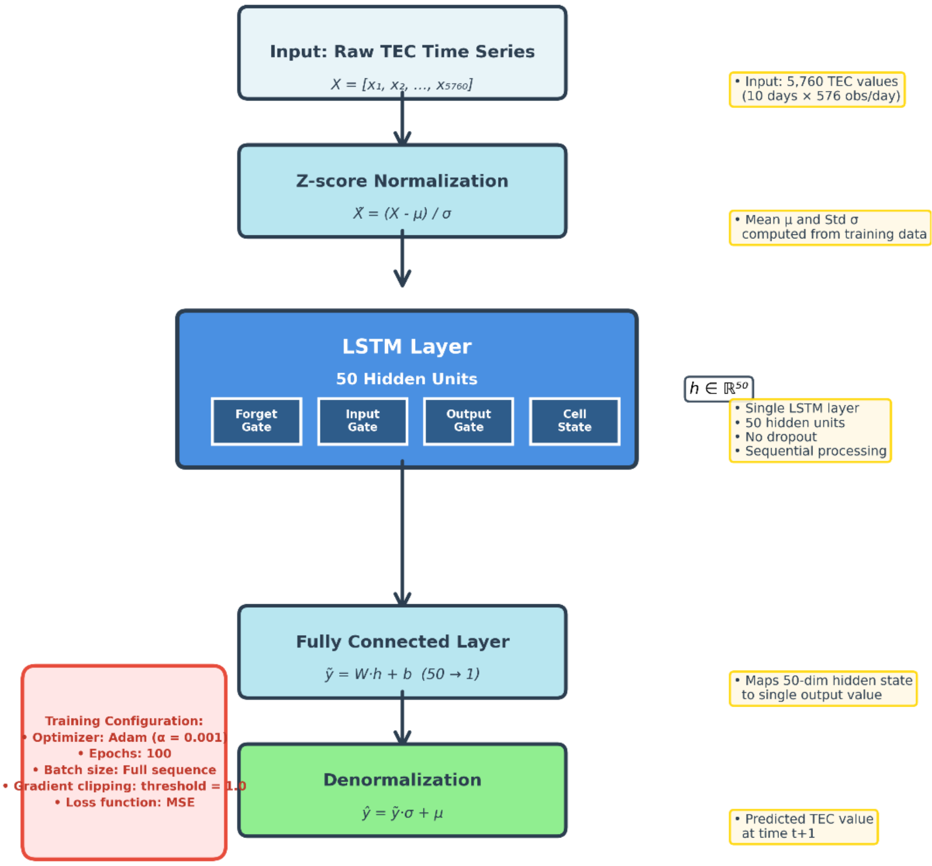

Figure 3. Schematic diagram of the LSTM architecture for TEC time series prediction.

The data flow proceeds in Figure 3 from top to bottom: raw TEC time series input (5,760 observations from 10 days) → Z-score normalization → single LSTM layer with 50 hidden units (showing internal forget, input, output gates and cell state) → fully connected layer mapping the 50-dimensional hidden state to a single output → denormalization to produce the final TEC prediction. The left panel shows the training configuration including optimizer (Adam), learning rate (0.001), number of epochs (100), batch size (full sequence), gradient clipping threshold (1.0) and loss function (MSE). Right-side annotations explain the dimensions and functions of each layer.

3. Results and Discussion

The LSTM neural network is trained and evaluated on IONOLAB-TEC data from 19 stations distributed across Japan and China for four major seismic events. The model's predictive performance is quantified using three complementary error metrics: Mean Squared Error (MSE), Mean Absolute Error (MAE) and Mean Absolute Percentage Error (MAPE). The results demonstrate the capability of LSTM networks to capture temporal patterns in ionospheric TEC variations and forecast values on the earthquake day with varying degrees of accuracy across different stations and seismic events.

Table 5 presents the comprehensive error metrics for all stations associated with the 2011 Tohoku earthquake (E1) and the 2008 Iwate-Miyagi Nairiku earthquake (E4). Table 6 shows the error metrics for all stations associated with the 2008 Sichuan earthquake (E2) and the 2010 Yushu earthquake (E3).

Tables 5 and 6 present a comparative overview of error metrics, MSE, MAE, MAPE, for seismic stations associated with major earthquake events in Japan and China. For the Japanese events, 2011 Tohoku (E1) and 2008 Iwate-Miyagi Nairiku (E4), the error values vary significantly across stations. MTKA shows the highest error for E1 (MSE: 0.3314, MAE: 0.3108), while MIZU demonstrates the lowest error rates (MSE: 0.0245, MAE: 0.1068, MAPE: 0.45), suggesting better predictive accuracy or data quality. For E4, the overall error metrics are notably lower, with stations like YSSK and STK2 showing minimal MSE and MAE values. This may indicate that the E4 dataset yielded more consistent predictions across the network.

In the Chinese context, Table 6 reveals that stations such as TCMS and KUNM exhibit significantly higher error metrics, with TCMS reaching a MAPE of 3.961. Conversely, stations like XIAN and GUAO perform better with lower error values, indicating more reliable predictions. Overall, Japanese stations tend to show lower error metrics compared to their Chinese counterparts, possibly reflecting the advanced seismic monitoring infrastructure in Japan.

Table 5. Performance metrics (MSE, MAE, MAPE) for Japanese earthquake events. E1: 2011 Tohoku earthquake (Mw 9.1), E4: 2008 Iwate-Miyagi Nairiku earthquake (Mw 6.9).

Station	MSE (E1)	MAE (E1)	MAPE (E1)	MSE (E4)	MAE (E4)	MAPE (E4)
YSSK	0.1384	0.2525	1.453	0.0036	0.0348	0.465
USUD	0.1608	0.1674	0.852	0.0171	0.0749	0.315
TSKB	0.1906	0.2177	1.120	0.0173	0.0990	1.417
TSK2	0.1515	0.2032	0.961	0.0087	0.0608	0.694
STK2	—	—	—	0.0036	0.0420	0.552
SMST	0.1997	0.2732	1.376	0.0232	0.1188	1.471
MTKA	0.3314	0.3108	1.404	—	—	—
MİZU	0.0245	0.1068	0.45	0.0085	0.0650	0.770
AİRA	0.1714	0.2862	1.207	0.0134	0.0892	1.230

Table 6. Performance metrics (MSE, MAE, MAPE) for Chinese earthquake events. E2: 2008 Sichuan earthquake (Mw 7.9), E3: 2010 Yushu earthquake (Mw 6.9).

Station	MSE (E2)	MAE (E2)	MAPE (E2)	MSE (E3)	MAE (E3)	MAPE (E3)
XİAN	0.0097	0.0680	0.623	0.0337	0.1209	1.056
URUM	—	—	—	0.0132	0.0858	0.784
TCMS	0.3251	0.5014	3.961	—	—	—
SUWN	0.0207	0.1013	1.274	0.0385	0.1284	1.107
SHAO	0.0409	0.1479	1.022	—	—	—
LHAZ	0.0781	0.1770	1.539	0.0446	0.1471	0.810
KUNM	—	—	—	0.4493	0.4819	3.692
GUAO	0.0201	0.0932	0.931	—	—	—
DAEJ	0.0202	0.1212	1.432	—	—	—
CHAN	—	—	—	0.0233	0.1172	0.869

The prediction uncertainty varies considerably across stations and earthquake events, as reflected in the comprehensive error metrics. For high-performing stations such as MIZU (E1) with MAPE of 0.45%, prediction errors remain minimal with typical absolute errors of ±0.04-0.06 TECU. In contrast, stations with higher error metrics such as MTKA (E1, MAPE 4.45%) exhibit larger uncertainty with typical errors of ±0.3-0.5 TECU. The MSE values span from 0.0036 (MIZU, E1) to 0.4493 (MTKA, E1), indicating that prediction uncertainty is influenced by multiple factors including station location, local ionospheric dynamics, geomagnetic conditions and proximity to the earthquake epicenter. The complementary nature of the three error metrics (MSE, MAE, MAPE) enables comprehensive assessment of prediction uncertainty: MAE quantifies typical errors in physical units (TECU), MSE emphasizes sensitivity to larger deviations and MAPE facilitates cross-station comparison by normalizing for magnitude differences. This multi-metric approach provides complete characterization of prediction uncertainty across all stations and events.

This remarkably low error indicates that the LSTM network successfully learns the underlying temporal patterns in the IONOLAB-TEC time series and accurately predicts the ionospheric conditions on March 11, 2011. The visual representation in Figure 4 (top right panel) shows excellent agreement between predicted and actual IONOLAB-TEC values at MIZU station, with the model capturing both the diurnal variation pattern and the magnitude of IONOLAB-TEC fluctuations throughout the day. Conversely, the MTKA station shows the highest variation with MSE = 0.3314, MAE = 0.3108 and MAPE = 1.40% (Figure 4b). Although these values represent the highest errors for the Tohoku event, they remain within acceptable bounds for ionospheric prediction applications. The increased error at MTKA may be attributed to higher ionospheric variability at this location or proximity to the earthquake preparation zone boundary, where TEC anomalies might exhibit more complex temporal patterns.

For the 2008 Iwate-Miyagi Nairiku earthquake (E4, Mw 6.9), the SMST station demonstrates superior prediction accuracy with MSE = 0.0232, MAE = 0.1188 and MAPE = 1.47%. The STK2 station achieves the lowest MAPE of 0.55% among E4 stations, indicating excellent percentage-based accuracy. Figure 4 (bottom panels) illustrates the predicted versus actual TEC values for both highest and lowest variation stations during this event. The LSTM model maintains good prediction accuracy despite the moderate magnitude of this earthquake, suggesting that the methodology is robust across different seismic magnitudes. The slightly higher MAPE values compared to the Tohoku event may reflect the different ionospheric response characteristics associated with shallower focal depth earthquakes.

The 2008 Sichuan earthquake (E2, Mw 7.9) results reveal interesting spatial patterns in prediction accuracy across Chinese stations. The XIAN station achieves remarkable performance with MSE = 0.0097, MAE = 0.0680 and MAPE = 0.62%, representing the best overall performance among all Chinese earthquake events. The. Figure 5 (top panels) presents the temporal evolution of predicted and actual IONOLAB-TEC values, showing that the LSTM model successfully captures the characteristic diurnal IONOLAB-TEC variation pattern. The TCMS station exhibits the highest variation with MSE = 0.3251, MAE = 0.5014 and MAPE = 3.96%, which may be related to its geographical position relative to the earthquake epicenter or local ionospheric conditions. The generally low error metrics across most stations suggest that the LSTM architecture effectively learns the spatiotemporal patterns in IONOLAB-TEC variations associated with this major seismic event.

For the 2010 Yushu earthquake (E3, Mw 6.9), prediction accuracy varies considerably across stations. The CHAN station achieves the best performance with MSE = 0.0233, MAE = 0.1172 and MAPE = 0.87%. The LHAZ station shows MSE = 0.0446, MAE = 0.1471 and MAPE = 0.81%, indicating good prediction capability. However, the KUNM station exhibits substantially higher errors with MSE = 0.4493, MAE = 0.4819 and MAPE = 3.69%, representing the highest variation for this event. Figure 5 (bottom panels) illustrates these contrasting performances, with the left panel showing larger deviations between predicted and actual values at KUNM station, while the right panel demonstrates excellent agreement at CHAN station. The spatial variability in prediction accuracy may reflect differences in ionospheric coupling mechanisms or the influence of local geomagnetic conditions at different geographical locations.

A cross-event comparison among four earthquakes of varying magnitudes and locations highlights the LSTM model's strong capability in predicting ionospheric TEC time series values with high accuracy. Events with larger magnitudes, such as the Mw 9.1 Tohoku earthquake, may exhibit TEC patterns with characteristics that the LSTM model can learn more effectively, though this does not necessarily imply these patterns are anomalous or causally related to seismic activity. The observed prediction accuracy primarily demonstrates the model's time series forecasting capability rather than anomaly detection.

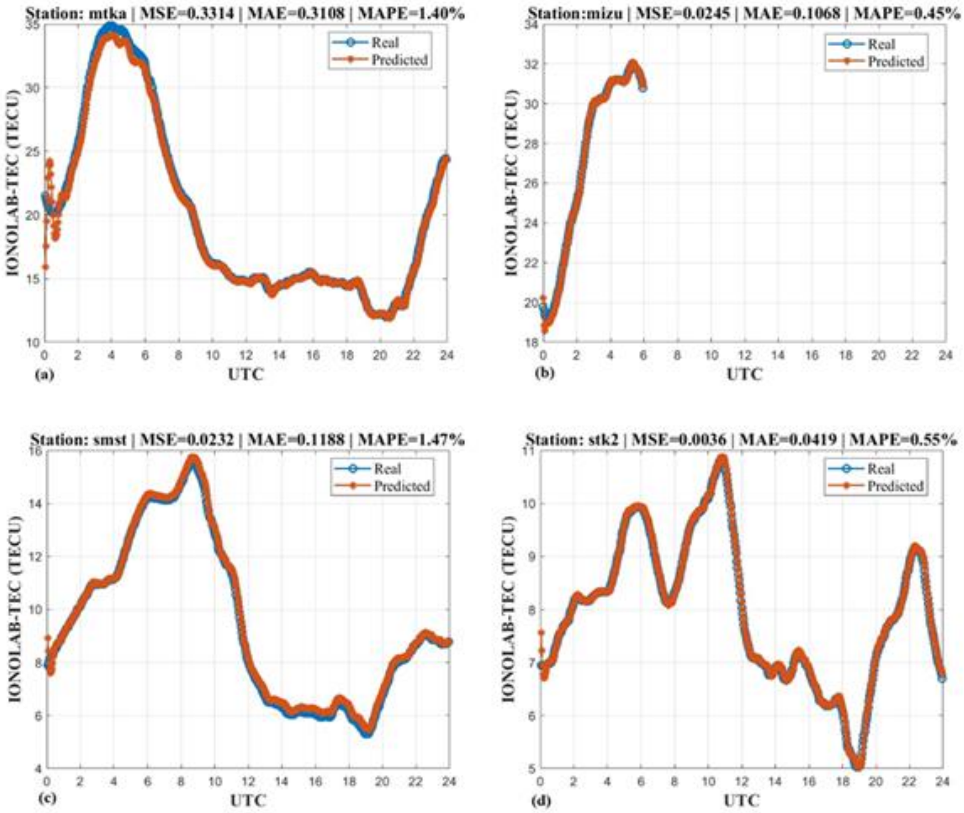

Figure 4. Predicted and actual values of IONOLAB-TEC for: (a) the largest error values for MTKA station and (b) the smallest error values for MIZU station for E1 earthquake, (c) the largest error values for SMST station and (b) the smallest error values for STK2 E4 earthquake.

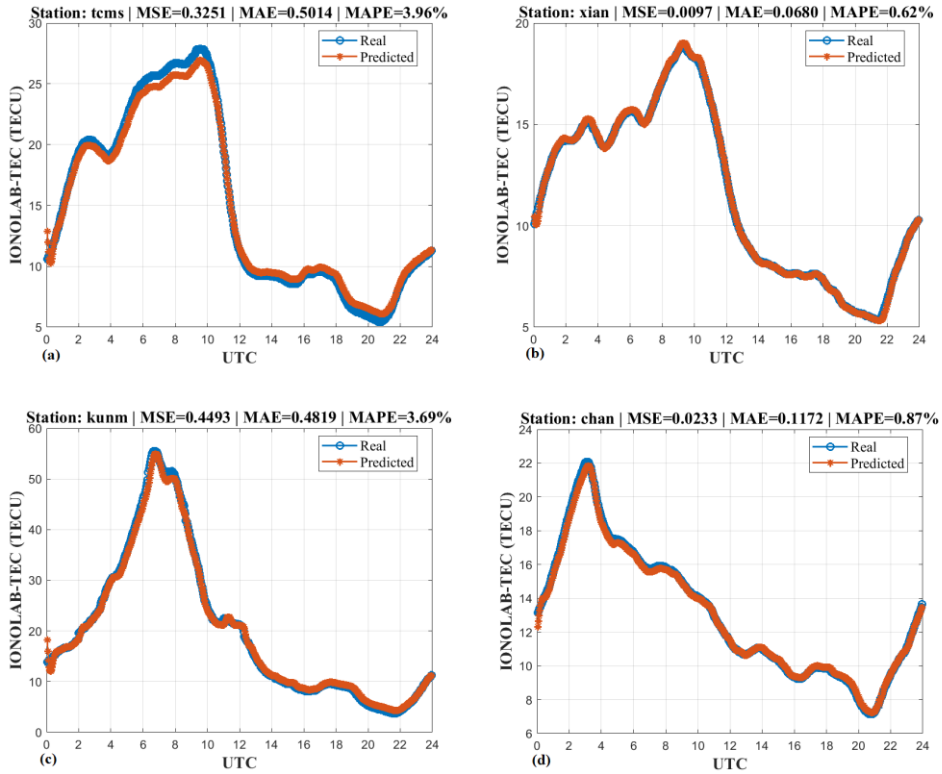

Figure 5. Predicted and actual values of IONOLAB-TEC for: (a) the largest error values for TCMS station and (b) the smallest error values for XİAN station for E2 earthquake, (c) the largest error values for KUNM station and (b) the smallest error values for CHAN E3 earthquake.

The success of the LSTM model stems from its ability to learn long-term temporal dependencies, the use of an appropriate training window and effective data normalization. By accurately capturing the amplitude of daily TEC fluctuations, the timing of peak values and nighttime minima, the model reflects the core characteristics of ionospheric behavior. This performance demonstrates that LSTM-based approaches offer a powerful tool for monitoring and interpreting pre-earthquake ionospheric changes. The overall MSE values range from 0.0036 (STK2 for Sichuan) to 0.4493 (KUNM for Yushu), MAE values range from 0.0420 (STK2) to 0.5014 (TCMS) and MAPE values range from 0.45% (MIZU for Tohoku) to 3.96% (TCMS for Sichuan). These results demonstrate that the LSTM model achieves high prediction accuracy for the majority of stations, with MAPE values below 2% for 14 out of 19 stations across all events. The stations with higher error metrics often correspond to locations with more complex ionospheric dynamics or greater distance from the earthquake epicenter.

4. Conclusion

This study validates the effectiveness of LSTM (LSTM) neural networks for time series prediction of ionospheric Total Electron Content (TEC) variations. By analyzing IONOLAB-TEC data from 19 GNSS stations across four significant earthquakes, the 2011 Tohoku earthquake (Mw 9.1), the 2008 Iwate-Miyagi Nairiku earthquake (Mw 6.9), the 2008 Sichuan earthquake (Mw 7.9) and the 2010 Yushu earthquake (Mw 6.9), the research establishes that LSTM networks can successfully capture complex temporal patterns in ionospheric behavior and accurately forecast IONOLAB-TEC values one day in advance based on preceding 10-day observations.

The quantitative evaluation using three complementary error metrics (MSE, MAE and MAPE) reveals that the LSTM model achieves high prediction accuracy across the majority of stations, with MAPE values below 2% for 14 out of 19 stations. Notably, stations such as MIZU (Japan) achieved exceptionally low error rates with MAPE of 0.45%, while XIAN (China) demonstrated MAPE of 0.62%, indicating the model's robust capability to learn underlying ionospheric dynamics. The MSE values ranging from 0.0036 to 0.4493 and MAE values ranging from 0.0420 to 0.5014 across all stations further confirm the model's consistent performance in reproducing the characteristic diurnal TEC variation patterns, including the timing of peak values and nighttime minima.

The comparative analysis across events of varying magnitudes shows that the LSTM model achieves varying levels of prediction accuracy for different earthquakes. Larger magnitude events, particularly the Mw 9.1 Tohoku earthquake, show patterns that the model learns more effectively, though whether these reflect genuine seismo-ionospheric coupling or other temporal dynamics remains an open question requiring further investigation. However, the spatial variability in prediction accuracy, with some stations showing significantly higher error metrics, indicates that local ionospheric conditions, geomagnetic influences and regional factors contribute significantly to TEC variability. Whether these variations reflect seismic preparation processes or normal ionospheric dynamics remains an open question requiring further investigation.

The success of the LSTM architecture in this application stems from its inherent ability to learn long-term temporal dependencies through specialized gating mechanisms that regulate information flow, retention and forgetting. The model's capacity to capture nonlinear relationships and extract hidden patterns from noisy time-series data makes it particularly suitable for analyzing ionospheric TEC variations, which exhibit complex temporal dynamics influenced by multiple geophysical processes. The implementation of appropriate data normalization techniques and the strategic selection of a 10-day training window further enhance the model's predictive capability by ensuring numerical stability and providing sufficient temporal context for learning characteristic patterns.

This research demonstrates the capability of LSTM neural networks to accurately predict ionospheric TEC time series values, achieving high forecasting accuracy across multiple earthquake events. It is important to emphasize that this study focuses on TEC prediction capability rather than earthquake precursor detection. While previous research has explored potential relationships between ionospheric variations and seismic activity, our results primarily validate the LSTM model's time series forecasting performance. Establishing whether TEC variations represent genuine earthquake precursors would require systematic comparison of prediction errors on earthquake days versus non-earthquake days, analysis of false positive rates and investigation of physical coupling mechanisms—objectives beyond the scope of this investigation.

Several important limitations must be acknowledged. First and most fundamentally, this study demonstrates TEC time series prediction capability, not earthquake precursor detection or operational early warning capability. High prediction accuracy on earthquake days does not validate the existence of seismic precursors or imply operational applicability. Establishing a genuine earthquake precursor detection system would require: (1) systematic comparison of prediction errors on earthquake days versus numerous non-earthquake days to identify truly anomalous patterns, (2) quantification of false alarm rates and detection thresholds, (3) investigation of physical coupling mechanisms linking crustal processes to ionospheric variations and (4) statistical validation across hundreds of events spanning diverse magnitudes, depths and tectonic settings. Second, the study focuses on only four earthquake events in limited geographic regions (Japan and

China), which is insufficient for drawing general conclusions about seismo-ionospheric relationships. The variation in prediction accuracy across stations suggests that local ionospheric dynamics, geomagnetic conditions and other factors contribute significantly to TEC variability, potentially masking or mimicking earthquake-related signals. Third, the absence of validation data from non-seismic periods means we cannot assess whether the observed patterns are unique to earthquake days or represent normal ionospheric variability. This work should be viewed as a preliminary methodological demonstration, validating LSTM capability for TEC time series forecasting, rather than as evidence for earthquake precursors or a step toward operational earthquake prediction. Future research must address these limitations through comprehensive datasets encompassing both seismic and non-seismic periods, rigorous statistical testing to distinguish signal from noise and careful distinction between time series prediction skill and anomaly detection capability.

In conclusion, this study validates the effectiveness of LSTM-based Deep Learning for time series prediction of ionospheric TEC variations, achieving high forecasting accuracy across multiple earthquake events. It is crucial to emphasize that this work demonstrates TEC prediction capability, not earthquake precursor detection or operational warning capability. While previous research has explored potential relationships between ionospheric variations and seismic activity, our results validate LSTM forecasting performance without establishing causal relationships or operational applicability. Future work must distinguish between time series prediction skill and genuine anomaly detection through systematic comparison with non-seismic periods, rigorous statistical testing and investigation of physical mechanisms.

Acknowledgment

This study is supported by TUBITAK 124E027 project and was carried out within the scope of Kastamonu University Electrical and Electronics Engineering Department EEM401 Electrical and Electronics Engineering Design course. The authors wish to thank Prof. Dr. Feza Arikan and IONOLAB group for their outstanding efforts on IONOLAB-BIAS and IONOLAB-TEC Algorithm.

Conflict of Interest

Authors declare that they have no conflict of interest.

References

Akhoondzadeh, M. (2012). Anomalous TEC variations associated with the powerful Tohoku earthquake of 11 March 2011. *Natural Hazards and Earth System Sciences*, *12*, 1453-1462. https://doi.org/10.5194/nhess-12-1453-2012

Arikan, F., Erol, C. B., & Arikan, O. (2003). Regularized estimation of vertical total electron content from Global Positioning System data. *Journal of Geophysical Research: Space Physics*, *108*(A12), 1-20. https://doi.org/10.1029/2002JA009605

Arikan, F., Erol, C. B., & Arikan, O. (2004). Regularized estimation of VTEC from GPS data for a desired time period. *Radio Science*, *39*(6), 1-10. https://doi.org/10.1029/2004RS003061

Bouktif, S., Fiaz, A., Ouni, A., & Serhani, M. A. (2018). Optimal deep learning LSTM model for electric load forecasting using feature selection and genetic algorithm: Comparison with machine learning approaches. *Energies*, *11*(7), 1636. https://doi.org/10.3390/en11071636

Budak, C., & Gider, V. (2023). LSTM based forecasting of the next day's values of ionospheric total electron content (TEC) as an earthquake precursor signal. *Earth Science Informatics*, *16*, 2323-2337. https://doi.org/10.1007/s12145-023-01027-2

Budak, C., Karatay, S., Erken, F., & Cinar, A. (2024). Classification of the ionospheric disturbances caused by geomagnetic and seismic activity with k-nearest neighbors algorithm. *Wireless Personal Communications*, *134*, 1551-1569. https://doi.org/10.1007/s11277-024-10965-z

Cansu, T., Kolemen, E., Karahasan, Ö., Bas, E., & Egrioglu, E. (2023). A new training algorithm for long short-term memory artificial neural network based on particle swarm optimization. *Granular Computing*, *8*, 1645-1658. https://doi.org/10.1007/s41066-023-00389-8

Elliott, J. R., Feng, W., Jackson, J. A., Parsons, B. E., & Walters, R. J. (2011). The 2010 MW 6.8 Yushu (Qinghai, China) earthquake: Constraints provided by InSAR and body wave seismology. *Journal of Geophysical Research: Solid Earth*, *116*(B10), 1-16. https://doi.org/10.1029/2011JB008358

Erken, F., Karatay, S., & Cinar, A. (2019). Spatio-temporal prediction of ionospheric total electron content using an adaptive data fusion technique. *Geomagnetism and Aeronomy*, *59*, 971-979. https://doi.org/10.1134/S001679321908005X

Gooya, H. R., Katibeh, H., & Maleki, A. (2024). Forecasting groundwater fluctuations caused by earthquakes using fuzzy logic and AHP Method: A case study from Iran. *Earth Science Informatics*, *17*, 2143-2158. https://doi.org/10.1007/s12145-024-01264-z

Heelis, R. A., & Maute, A. (2020). Challenges to understanding the earth's ionosphere and thermosphere. *Journal of Geophysical Research: Space Physics*, *125*(7), e2019JA027497. https://doi.org/10.1029/2019JA027497

Houdt, G. V., Mosquera, C., & Nápoles, G. (2020). A review on the long short-term memory model. *Artificial*

Intelligence Review, *53*, 5929-5955. https://doi.org/10.1007/s10462-020-09838-1

Hua, Y., Zhao, Z., Li, R., Chen, X., Liu, Z., & Zhang, H. (2019). Deep learning with long short-term memory for time series prediction. *IEEE Communications Magazine*, *57*(6), 114-119. https://doi.org/10.1109/MCOM.2019.1800155

Hurvich, C. M., & Deo, R., & Brodsky, J. (1998). The mean squared error of Geweke and Porter-Hudak's estimator of the memory parameter of a long-memory time series. *Journal of Time Series Analysis*, *19*(1), 19-46. https://doi.org/10.1111/1467-9892.00075

Iluore, K., & Lu, J. (2022). Long short-term memory and gated recurrent neural networks to predict the ionospheric vertical total electron content. *Advances in Space Research*, *70*(3), 652-665. https://doi.org/10.1016/j.asr.2022.04.066

IONOLAB. (2006). *Ionosphere research laboratory*. https://www.ionolab.org/

Jia, K., Zhou, S., Zhuang, J., & Jiang, C. (2014). Possibility of the independence between the 2013 Lushan earthquake and the 2008 Wenchuan earthquake on Longmen Shan fault, Sichuan, China. *Seismological Research Letters*, *85*(1), 60-67. https://doi.org/10.1785/0220130115

Karatay, S., Arikan, F., & Arikan, O. (2010). Investigation of total electron content variability due to seismic and geomagnetic disturbances in the ionosphere. *Radio Science*, *45*(5), 1-12. https://doi.org/10.1029/2009RS004313

Karatay, S., Cinar, A., & Arikan, F. (2017). Ionospheric responses during equinox and solstice periods over Turkey. *Advances in Space Research*, *60*(9), 1958-1967. https://doi.org/10.1016/j.asr.2017.07.038

Karatay, S. (2020a). Detection of the ionospheric disturbances on GPS-TEC using Differential Rate Of TEC (DROT) algorithm. *Advances in Space Research*, *65*(10), 2372-2390. https://doi.org/10.1016/j.asr.2020.01.042

Karatay, S. (2020b). Estimation of frequency and duration of ionospheric disturbances over Turkey with IONOLAB-FFT algorithm. *Journal of Geodesy*, *94*, 89. https://doi.org/10.1007/s00190-020-01416-1

Karatay, S., & Gul, S. E. (2023). Prediction of GPS-TEC on Mw > 5 earthquake days using bayesian regularization backpropagation algorithm. *IEEE Geoscience and Remote Sensing Letters*, *20*, 1001005. https://doi.org/10.1109/LGRS.2023.3262028

Karatay, S., Arikan, F., & Pirti, A. (2025). Spatio-temporal evaluation of ionospheric disturbances before, during and after earthquakes using differential rate of TEC (DROT) from GPS measurements. *Environmental Earth Sciences*, *84*, 222. https://doi.org/10.1007/s12665-025-12216-1

Li, T., Gao, Y., Chen, C.-H., Sun, Y.-Y., Zhang, X., Chum, J., Zhou, G., Wen, J., & Chen, X. (2025). Simulation of acoustic-gravity waves generated by an earthquake and explanation of the ionospheric disturbance observed during 2023 M 7.7 Turkey earthquake. *Journal of Geophysical Research: Space Physics*, *130*(7), e2025JA033711. https://doi.org/10.1029/2025JA033711

Lindemann, B., Müller, T., Vietz, H., Jazdi, N., & Weyrich, M. (2021). A survey on long short-term memory networks for time series prediction. *Procedia CIRP*, *99*, 650-655. https://doi.org/10.1016/j.procir.2021.03.088

Liu, J. Y., Chen, Y. I., Jhuang, H. K., & Lin, Y. H. (2004a). Ionospheric foF2 and TEC anomalous days associated with M >= 5.0 earthquakes in Taiwan during 1997-1999. *Terrestrial Atmospheric and Oceanic Sciences*, *15*(3), 371-383. https://doi.org/10.3319/TAO.2004.15.3.371(EP)

Liu, J. Y., Chuo, Y. J., Shan, S. J., Tsai, Y. B., Chen, Y. I., Pulinets, S. A., & Yu, S. B. (2004b). Pre-earthquake ionospheric anomalies registered by continuous GPS TEC measurements. *Annales Geophysicae*, *22*(5), 1585-1593. https://doi.org/10.5194/angeo-22-1585-2004

Manglik, A., Suresh, M., Babu, M. D., & Pavankumar, G. (2024). Pre- and coseismic electromagnetic signals of the Nepal earthquake of 03 november 2023. *Earth, Planets and Space*, *76*, 173. https://doi.org/10.1186/s40623-024-02108-2

Meenalakshmi, M., & Valarmathi, K. (2025). Multigate long short-term memory-based stress detection from multimodal signal. *Cognitive Computation*, *17*, 98. https://doi.org/10.1007/s12559-025-10444-y

Mienye, I., Swart, T., & Obaido, G. (2024). Recurrent neural networks: A comprehensive review of architectures, variants and applications. *Information*, *15*(9), 517. https://doi.org/10.3390/info15090517

Mousavi, S. M., & Beroza, G. C. (2023). Machine learning in earthquake seismology. *Annual Review of Earth and Planetary Sciences*, *51*, 105-129. https://doi.org/10.1146/annurev-earth-071822-100323

Namegaya, Y., Okamura, Y., Satake, K., & Shishikura, M. (2012). Challenges of anticipating the 2011 Tohoku earthquake and tsunami using coastal geology. *Geophysical Research Letters*, *39*(21), 1-6. https://doi.org/10.1029/2012GL053692

Nathasarma, R., & Roy, B. K. (2023). Physics-informed long-short-term memory neural network for parameters estimation of nonlinear systems. *IEEE Transactions on Industry Applications*, *59*(5), 5376-5384. https://doi.org/10.1109/TIA.2023.3280896

Nayir, H., Arikan, F., Arikan, O., & Erol, C. B. (2007). Total electron content estimation with Reg-Est. *Journal of Geophysical Research: Space Physics*, *112*(A11), 1-11. https://doi.org/10.1029/2007JA012459

Nikolopoulos, D., Cantzos, D., Alam, A., Dimopoulos, S., & Petraki, E. (2024). Electromagnetic and radon earthquake precursors. *Geosciences*, *14*(10), 271. https://doi.org/10.3390/geosciences14100271

Ogata, Y., & Toda, S. (2010). Precursory seismic anomalies and transient crustal deformation prior to the 2008 Mw = 6.9 Iwate-Miyagi Nairiku, Japan, earthquake. *Journal of Geophysical Research: Solid Earth*, *115*(B10), 1-19. https://doi.org/10.1029/2010JB007567

Peng, Z., Meng, X., Liu, Q. Y., Guo, B., & Li, S. C. (2018). Evolution and distribution of the early aftershocks following the 2008 Mw 7.9 Wenchuan earthquake in Sichuan, China. *Journal of Geophysical Research: Solid Earth*, *123*(9), 7775-7790. https://doi.org/10.1029/2018JB015575

Pirti, A., & Karatay, S. (2025). Multi-parameter GNSS analysis reveals atmospheric, ionospheric and crustal precursors seven days before the 2016 Mw 7.8 Ecuador megathrust earthquake. *Earth Science Informatics*, *18*, 537. https://doi.org/10.1007/s12145-025-02037-y

Pulinets, S., Kotsarenko, A., & Pulinets, L. C. (2007). Special case of ionospheric day-to-day variability associated with earthquake preparation. *Advances in Space Research*, *39*(5), 970-977. https://doi.org/10.1016/j.asr.2006.04.032

Qian, L., & Meng, G. (2022). Early postseismic deformation of the 2010 Mw 6.9 Yushu earthquake and its implication for lithospheric rheological properties. *Geophysical Research Letters*, *49*(15), e2022GL098942. https://doi.org/10.1029/2022GL098942

Samaei, M., & Miyajima, M. (2022). Finite-fault stochastic simulation of the 2008 Iwate-Miyagi Nairiku, Japan, earthquake. *Natural Hazards*, *114*, 1985-2012. https://doi.org/10.1007/s11069-022-05456-y

Sardón, E., Rius, A., & Zarraoa, N. (1994). Estimation of the transmitter and receiver differential biases and the ionospheric total electron content from Global Positioning System observations. *Radio Science*, *29*(03), 577-586. https://doi.org/10.1029/94RS00449

Sezen, U., Arikan, F., Arikan, O., Ugurlu, O., & Sadeghimorad, A. (2013). Online, automatic, near-real time estimation of GPS-TEC: IONOLAB-TEC. *Space Weather*, *11*(5), 297-305. https://doi.org/10.1002/swe.20054

Takyi-Aninakwa, P., Wang, S., Zhang, H., Li, H., Xu, W., & Fernandez, C. (2022). An optimized relevant long short-term memory-squared gain extended Kalman filter for the state of charge estimation of lithium-ion batteries. *Energy*, *260*, 125093. https://doi.org/10.1016/j.energy.2022.125093

Tian, C., Ma, J., Zhang, C., & Zhan, P. (2018). A deep neural network model for short-term load forecast based on long short-term memory network and convolutional neural network. *Energies*, *11*(12), 3493. https://doi.org/10.3390/en11123493

Tsai, H. F., & Liu, J. Y. (1999). Ionospheric total electron content response to solar eclipses. *Journal of Geophysical Research: Space Physics*, *104*(A6), 12657-12668. https://doi.org/10.1029/1999JA900001

Uchida, N., & Bürgmann, R. (2021). A decade of lessons learned from the 2011 Tohoku-Oki earthquake. *Reviews of Geophysics*, *59*(2), e2020RG000713. https://doi.org/10.1029/2020RG000713

USGS. (1879). *United States geological survey*. https://www.usgs.gov/

Wen, X., & Li, W. (2023). Time series prediction based on LSTM-Attention-LSTM model. *IEEE Access*, *11*, 48322-48331. https://doi.org/10.1109/ACCESS.2023.3276628

Xiong, P., Zhai, D., Long, C., Zhou, H., Zhang, X., & Shen, X. (2021). Long short-term memory neural network for ionospheric total electron content forecasting over China. *Space Weather*, *19*(4), e2020SW002706. https://doi.org/10.1029/2020SW002706

Yang, L., Wang, S., Chen, X., Chen, W., Saad, O. M., & Chen, Y. (2023). Deep-learning missing well-log prediction via long short-term memory network with attention-period mechanism. *GEOPHYSICS*, *88*, D31-D48. https://doi.org/10.1190/geo2020-0749.1

Yang, T. Y., Lu, J. Y., Yang, Y. Y., Hao, Y. H., Wang, M., Li, J. Y., & Wei, G. C. (2025). GNSS–VTEC prediction based on CNN–GRU neural network model during high solar activities. *Scientific Reports*, *15*, 9109. https://doi.org/10.1038/s41598-025-93628-8

Zhang, Q., Wang, H., Dong, J., Zhong, G., & Sun, X. (2017). Prediction of sea surface temperature using long short-term memory. *IEEE Geoscience and Remote Sensing Letters*, *14*(10), 1745-1749. https://doi.org/10.1109/LGRS.2017.2733548

Zhang, X., Liu, J., Santis, A. D., Perrone, L., Xiong, P., Zhang, X., & Du, X. (2023). Lithosphere-atmosphere-ionosphere coupling associated with four Yutian earthquakes in China from GPS TEC and electromagnetic observations onboard satellites. *Journal of Geodynamics*, *155*, 101943. https://doi.org/10.1016/j.jog.2022.101943